photonics

Article

Comprehensive Analysis of Optical Resonances and Sensing Performance in Metasurfaces of Silicon Nanogap Unit

Masanobu Iwanaga

Research Center for Electronic and Optical Materials, National Institute for Materials Science (NIMS), 1-1 Namiki, Tsukuba 305-0044, Japan; iwanaga.masanobu@nims.go.jp

Abstract: Metasurfaces composed of silicon nanogap units have a variety of optical resonances, including bound states in the continuum (BIC). We show comprehensive numerical results on metasurfaces of Si-nanogap units, analyze the optical resonances, and clarify optically prominent resonances as well as symmetry-forbidding resonances that are the BIC, based on the numerical analyses of optical spectra and resonant electromagnetic field distributions. Introducing asymmetry in the unit cell, the BIC become optically allowed, being identified as magnetic dipole, electric quadrupole, and magnetic quadrupole resonances. Moreover, the optical resonances are examined in terms of refractive index sensing performance. A pair of the resonances associated with electric field localization at the nanogap was found to be sensitive to the refractive index in contact with the metasurfaces. Consequently, the gap mode resonances are shown to be suitable for a wide range of refractive index sensing over 1.0–2.0.

Keywords: all-dielectric metasurface; silicon nanogap; BIC; optical sensing; refractive index

1. Introduction

Metasurfaces have opened the way for diverse optical properties and applications. In addition to light-wave manipulations employing the complex subwavelength structures [1–7], various types of resonances have been exploited to realize prominent effects that are helpful for practical applications such as metalenses [8–12], color splitting to pixel [13–15], liquid-crystal-based active responses [16], and biosensing based on resonance shift [17–19] and on fluorescence detection [20–23].

Among many effects in all-dielectric metasurfaces, one of the popular resonances is quasi-bound states in the continuum (qBIC). Structural asymmetry allows us to access the resonances of qBIC that are forbidden in symmetric structures. Although this concept was introduced in an electronic system almost a hundred years ago [24], a similar effect to the electronic system was shown in a nanophotonic system, which was a photonic crystal, about ten years ago [25], which stimulated nanophotonics studies on the qBIC.

As applications of the qBIC in nanophotonics, refractive index sensing [26–28] and nonlinear effects [29–31] were explored to date. On the physical limit of refractive index sensing using periodic structures, a formula for the resolution in the units of nm/refractive index unit (RIU) was recently shown [32] such that

$$\frac{\Delta\lambda}{\Delta n} = P \tag{1}$$

where λ, n, and P denote wavelength of light, refractive index of surrounding medium, and periodic length, respectively. Equation (1) indicates that the upper limit of refractive index sensing is determined by the periodic length P.

Figure 1 illustrates structural features of metasurfaces addressed in this study. In Figure 1a,b, Si-nanogap units are symmetric and asymmetric in the unit cell on the xy plane, respectively. Keeping gap width g constant, we vary y-width, y_1 and y_2, while

check for updates

Citation: Iwanaga, M. Comprehensive Analysis of Optical Resonances and Sensing Performance in Metasurfaces of Silicon Nanogap Unit. *Photonics* **2024**, *11*, 1053. https://doi.org/10.3390/photonics11111053

Received: 14 October 2024
Revised: 4 November 2024
Accepted: 8 November 2024
Published: 10 November 2024

keeping the sum of $y_1 + y_2 + g$ constant. In Figure 1b, a condition of $y_1 > y_2$ results in $-y$-direction offset of the center line in the nanogap (dotted line). We define the absolute value of the offset as α, which is an asymmetric parameter, and quantitatively characterize the asymmetry in the unit cell, and can write it down such that

$$\alpha = |y_1 - y_2|/2. \tag{2}$$

Introducing the asymmetry along only the y axis, the definition in Equation (2) is simple and explicitly expressed. Also, experimental tests in the future will be easy to conduct. Note that the asymmetric parameters for qBIC are usually normalized using a reasonable reference length to make the parameters dimensionless; for example, the offset can be normalized by the length of unit cell; however, to make the physical meaning of α clear, we simply define the α in Equation (2). Thus, the present α means the offset of the gap center from the center of unit cell; that is, $\alpha = 1$ means that the offset is 1 nm.

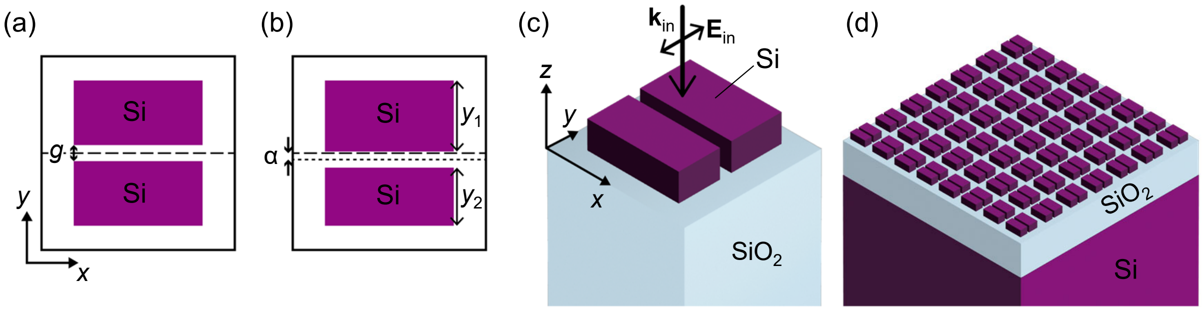

Figure 1. Schematics of metasurface structure and optical configuration in this study. (**a**) xy-section view of unit cell of metasurface of Si-nanogap unit (purple). The gap g is indicated with a both-end arrow. The center line along the x axis is drawn with a broken line, which goes across the central point of the unit cell. (**b**) Asymmetry introduced in the unit cell is indicated by a quantity α, which is offset from the center line (broken line) to the middle line (dotted line) in the gap. (**c**) Three-dimensional illustration of unit cell of metasurface of an asymmetric Si-nanogap pair. Optical configuration is shown together. The unit cells in (**a**–**c**) are set to have dimensions of 600×600 nm^2 in the xy plane. Length of the Si nanoblock along the x axis is 400 nm and the sum of $y_1 + y_2 + g$ is 400 nm. Height of the Si nanoblock is set to 200 nm. (**d**) Three-dimensional illustration of a metasurface of periodic array of asymmetric Si-nanogap units, which are assumed to be infinitely periodic in the computations.

In Figure 1c, a 3D illustration of the unit cell of the metasurface (Figure 1b) is shown together with spatial xyz coordinates and an optical configuration. Wavevector $\mathbf{k}_{\text{in}}$ denotes the wavevector of the incident plane wave, and vector $\mathbf{E}_{\text{in}}$ represents electric field (or polarization) of the incidence. In this study, we mainly study normal incidence because the asymmetry enables us to access qBIC and allows us to explore various optical resonances. The metasurface is schematically illustrated in Figure 1d, which is assumed to be infinitely periodic in the computations. In practice, the metasurface is designed to be fabricated through nanolithography on a Si-on-insulator (SOI) wafer.

2. Materials and Methods

The metasurfaces in this study are assumed to comprise dielectrics of Si and SiO_2. SOI substrates are assumed to be used as base materials to fabricate the Si metasurfaces. In particular, the thickness of the top SOI layer, the middle buried oxide layer that is SiO_2, and the base Si layer are set to 200 nm, 1000 nm, and 725 µm, respectively, in accordance with SOI substrates available in reality. The permittivity of crystalline Si was taken from the literature [33] and that of SiO_2 was set to a representative value of 2.1316 in the photon-energy range of present interest. Using these permittivities, realistic simulations were conducted.

Numerical implementation was conducted based on a method combining rigorously coupled-wave analysis (RCWA) [34], which solves Fourier-transformed Maxwell equations for infinitely periodic objects in the frequency domain, with the scattering-matrix (S-matrix) algorithm [35]. The S-matrix algorithm makes numerical calculations stable even for stacked layer structures. The combined numerical method is a frequency-domain method and suitable to precisely compute optical spectra such as reflectance and transmittance spectra of periodic structures; indeed, the method has been applied to reproduce experimental optical spectra in various periodically structured materials such as metamaterials and metasurfaces [36–41]. The code executing the RCWA and S-matrix algorithm run on supercomputers in a multiparallel implementation (MPI) manner. Optical spectra were computed in the MPI manner and therefore the net runtime was almost equal to total runtime/(number of MPI), being substantially reduced. Also, the combined method enables us to output electromagnetic (EM)-field distributions, which is helpful to understand features of optical resonances in the metasurfaces. The RCWA is mathematically exact to the Maxwell equation under infinite expansion of the Fourier series. In reality, the RCWA provides approximate solutions by truncating the Fourier series at a finite order. We set the truncation order at ± 15 and more in this study and did not see changes in the optical spectra. Note that, since we considered 2D periodic systems, the total truncation order was 31×31 and more.

3. Results

3.1. Asymmetric Metasurfaces and qBIC Modes

Figure 2a shows a series of reflectance spectra of metasurfaces of Si-nanogap units, illustrated Figure 1b–d. The reflectance is normalized and takes values in a range from 0 to 1. The reflectance spectra are displayed with offset; accordingly, the zero lines for the offset spectra are drawn with thin gray lines.

The unit cell is set to be 600×600 nm^2 in the xy plane, and the width of Si nanoblocks along the x axis is set to 400 nm. The height of Si nanoblocks along the z axis is 200 nm. The gap g between the Si nanoblocks is set to 50 nm, and the sum of $y_1 + y_2$ is set to 350 nm; consequently, the unit of Si nanoblocks has a dimension of 400×400 nm^2 in the xy plane, being set at the center of the unit cell.

Introducing the asymmetry represented by α, we can allow for the qBIC modes to appear in optical spectra, such as reflectance spectra in Figure 2a. The qBIC modes are indicated with MD, MQ, and EQ that denote magnetic dipole, magnetic quadrupole, and electric quadrupole, respectively, and are indicated with arrows. They appear for $\alpha \geq 1$ though the signals at $\alpha = 1$ are quite small. The refractive index n in the incident layer and gaps between the Si nanoblocks is set to 1.0. The Si-nanogap unit cell is anisotropic for x and y axes; accordingly, the reflectance spectra are also anisotropic. The x- and y-polarized reflectance spectra are shown from bottom to top with offset, using black-to-blue and red-to-brown colors, respectively. The parameter α varies from 0 to 25. The series of reflectance spectra exhibit definite anisotropy for the incident polarizations and various resonant responses in the shapes of the spectra. In the photon energy range over 1.41 eV, diffraction-associated resonant modes appear. We here focus on the resonances below 1.4 eV, which are diffraction-free and belong to a subwavelength range at the normal incidence.

We briefly mention a general aspect in optical systems (e.g., Figure 1c) that contain periodic structures and plain waves that are incoming and outgoing. Even when the periodic systems have inversion symmetry in the xy plane, oblique incidence to the xy plane yields asymmetry in the optical responses; consequently, qBIC modes can be observed under oblique incidence. In this study, we mainly study the normal incidence and make the plain waves symmetric in the xy plane; therefore, at the normal incidence, the qBIC modes are observed only for the metasurface of asymmetric units (i.e., $\alpha > 0$) that do not have inversion symmetry in the xy plane. Note that, under the oblique incidence, the optical systems are asymmetric for the xy plane, and that the origin of asymmetry is generally indistinguishable between the structural units and optical configurations.

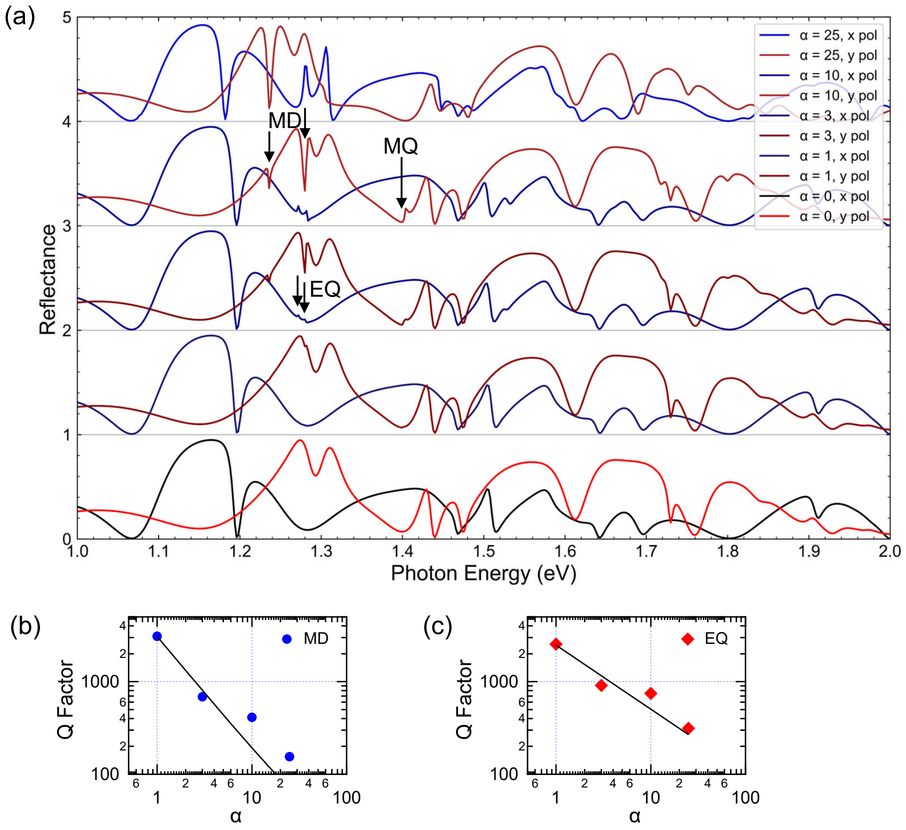

Figure 2. Optical resonances emerged in the Si-nanogap unit metasurfaces. (**a**) Computed reflectance spectra at two incident polarizations, $\mathbf{E}_{\text{in}} \parallel x$ and $\mathbf{E}_{\text{in}} \parallel y$ for various asymmetric parameters α, defined in Figure 1, and a fixed gap g of 50 nm. The reflectance spectra are shown with offset, changing color from black to blue for $\mathbf{E}_{\text{in}} \parallel x$ and from red to brown for $\mathbf{E}_{\text{in}} \parallel y$, in accordance with $\alpha = 0$–25, respectively. EQ, MD, and MQ denote electric quadrupole, magnetic dipole, and magnetic quadrupole, respectively, indicated by arrows. (**b**,**c**) Asymmetric parameter α and estimated quality (Q) factors of the MD (closed blue circles) and EQ modes (red diamonds), respectively. The Q factor is defined as Equation (3). Black lines denote fitted lines using a power function (see the text).

The reflectance spectra in Figure 2a have several peaks with broad bands at both x and y polarizations. The peaks coexist in the photon-energy range with interference coming from the multilayer structure of the SOI substrate; the interference is easy to be verified at a low energy range between 1.1 and 1.2 eV at x and y polarizations, respectively. These coexisting properties make the spectra complicated.

In addition, the spectra in Figure 2a include qBIC resonances with narrow line widths; the EQ modes are located at 1.2717 and 1.2809 eV for x polarization, the MD modes at 1.236 and 1.280 eV for y polarization, and the MQ modes at 1.403 eV for y polarization, as indicated by arrows. For smaller α, the resonant signals become smaller and finally disappear at $\alpha = 0$ for both polarizations, suggesting that these signals originate from qBIC. These resonances are quantified using quality (Q) factor, defined such that

$$Q = \frac{\omega_0}{\Delta\omega} \tag{3}$$

where ω_0 and $\Delta\omega$ denote resonant frequency and full width at the half maximum (FWHM) of the resonance in the frequency domain, respectively. In Figure 2b,c, the Q factors of MD (blue closed circle) and EQ modes (red diamond) are plotted for the parameter α, respectively. Although two MD and EQ lines appear, we chose the lower-energy resonance. The reason why the two MD modes appear is described with examining resonant EM-field distributions below. As the parameter α becomes smaller, the Q factors increase and exceed

1000 at $\alpha = 1$. The Q factor was fitted using a power function, $Q = A\alpha^n + B$, where A and B are constants, being found that $n = -1.22$ and -0.70 for the MD and EQ modes, respectively. The fitted power functions are shown with black lines. If radiative loss is simply assumed to evaluate the Q factors, a relation of $Q \propto \alpha^{-2}$ was suggested [42]. However, nonradiative losses are able to occur, due to light absorption by the constituent materials and surface roughness that could give rise to in nanofabrication processes, and substantially reduce the large Q factors over 1000 [43]. In the present numerical evaluations, the absorption loss is explicitly incorporated based on the permittivity of crystalline Si in the literature [33]. Furthermore, the high-Q modes are not isolated from the broad-band interference mode in the present metasurfaces; therefore, the EM-field confinement is considered to be reduced, though it is difficult to quantitatively evaluate the net amount of dissipation stemming from the interference mode.

Representative resonant EM-field distributions of qBIC are shown in Figure 3, where the asymmetric parameter α is chosen to be 10. EQ-mode EM-field distributions are shown in Figure 3a–c, where $|\mathbf{E}|$, $\mathrm{Re}(E_z)$, and $|\mathbf{H}|$ components are displayed, respectively. The boundaries of Si nanoblocks are shown with dotted white lines in Figure 3c. From the EM fields, several features are observed, as follows:

1. EM-field intensity is significantly enhanced on the resonance. For the incident intensities of $|\mathbf{E}_{\mathrm{in}}|^2 = 1$ and $|\mathbf{H}_{\mathrm{in}}|^2 = 1$, the maxima of $|\mathbf{E}|^2$ and $|\mathbf{H}|^2$ reach 420 and 841 in Figure 3a,c, respectively. Note that the nanogap does not contribute to the large EM-field enhancement in this mode.
2. The field pattern of $\mathrm{Re}(E_z)$ in Figure 3b indicates that the mode has quadratic oscillation on and around the Si-nanogap unit. Therefore, this mode is attributed to an EQ mode.
3. Anisotropy is introduced in the unit structure along the y axis and results in the anisotropy of the EM-field distributions, as observed in Figure 3a–c.
4. The resonant EM fields predominantly consist of near-field distributions in and around the Si-nanogap unit. As a result, the imaginary parts of EM fields contribute to the enhanced intensities. This is verified from the fact that the maximum of $|\mathrm{Re}(E_z)|$ in Figure 3b is approximately two-fold smaller than that of $|\mathbf{E}|$ in Figure 3a.

For y polarization, the qBIC modes are magnetic modes. Magnetic dipole resonance is visualized in Figure 3d–f, where $|\mathbf{E}|$, $|\mathbf{H}|$, and a snapshot of $\mathrm{Re}(H_z)$ are shown, respectively. Due to the nanogap between the two Si nanoblocks, strong localization of electric fields in the nanogap emerges, as shown in Figure 3d; accordingly, the magnetic fields are weaker at the center of the unit cell, as seen in Figure 3e; however, they exhibit a modified magnetic-dipole field distribution that is mainly localized in the Si domain, as shown in Figure 3f. Thus, the EM-field distributions retain a feature of magnetic-dipole resonance.

We here remark multipole approximations for the qBIC modes, which were reported frequently. First of all, it is to be noted that there is no analytical solution for the present metasurfaces that have complicated unit structures, in comparison with ideal spheres. Therefore, any trial to conduct multipole expansion for the metasurfaces will result in numerically approximated analyses. The issue is that it is difficult to evaluate the precision of the approximation in a quantitative manner. As shown in Figure 3d–i, the MD modes are significantly modified due to the nanogap and another mode of the gap mode coexists.As a result, if we should conduct the multipole expansion, the approximated multipolar values will be difficult to justify. Second, we already conducted and reported a multipole analysis for the Si-nanogap unit using a finite-element method [28]. A similar result is expected and is not repeated here. Instead, the information on the EM-field distributions is shown in Figure 3.

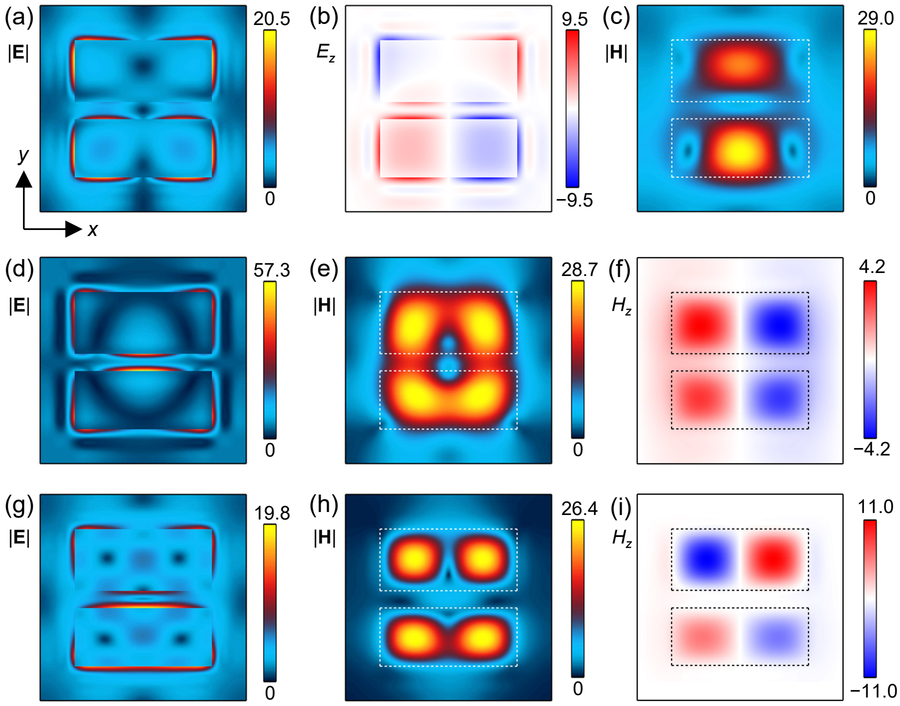

Figure 3. Resonant electromagnetic (EM)-field distributions on the qBIC resonances. (**a**) xy-section view of $|\mathbf{E}|$ distribution at 1.272 eV. The xy axes are shown together and the xy sections were taken at the half height of the Si-nanogap pair. These settings are in common with the other panels in this figure. (**b**) Snapshot of $\mathrm{Re}(E_z)$ component, corresponding to (**a**), presents a signature of electric quadrupole (EQ) mode. (**c**) $|\mathbf{H}|$ distribution, corresponding to (**a**). The incident polarization was set to be $\mathbf{E}_{\mathrm{in}} \parallel x$ in (**a**–**c**). (**d**–**f**) $|\mathbf{E}|$, $|\mathbf{H}|$, and $\mathrm{Re}(H_z)$ distributions at 1.236 eV, respectively. The magnetic-field distribution shows a signature of magnetic dipole (MD) mode. (**g**–**i**) $|\mathbf{E}|$, $|\mathbf{H}|$, and $\mathrm{Re}(H_z)$ distributions at 1.402 eV, respectively. The magnetic-field distribution shows a signature of magnetic quadrupole (MQ) mode. The incident polarization was set to be $\mathbf{E}_{\mathrm{in}} \parallel y$ in (**d**–**i**). The color bars indicate values of resonantly enhanced EM fields, when the absolute values of incident fields were set to unity, that is, $|\mathbf{E}_{\mathrm{in}}| = 1$ and $|\mathbf{H}_{\mathrm{in}}| = 1$.

In Figure 3d, the electric field is strongly localized in the nanogap and takes the maximum intensity at the center of x positions. In other words, the electric field is a single node in the nanogap along the x axis. We note that another MD mode in Figure 2a is located at a higher photon energy than this MD mode and has two maxima on the electric-field intensity in the nanogap; that is, it has two nodes in the nanogap. Thus, the two MD modes correspond to the first and second electric-field nodes in the nanogap. We mention that the third node is not induced because the length of the Si nanoblocks along the x axis is not enough. A similar type of resonances appears later (Section 3.2).

Magnetic quadrupole resonance is visualized in Figure 3g–i that shows $|\mathbf{E}|$, $|\mathbf{H}|$, and a snapshot of $\mathrm{Re}(H_z)$, respectively. The electric and magnetic field distributions show four minimum and maximum points in the Si domain, respectively, which indicates quadrupole. This feature is confirmed from the $\mathrm{Re}(H_z)$ distribution in Figure 3i.

Summing up Figure 3 briefly, the qBIC modes are found to be EQ, MD, and MQ modes. They have resonantly enhanced EM fields, that reach hundred-to-thousand-fold intensity, compared to that of incidence.

3.2. Resonant Shift for Refractive Index

Two series of numerically calculated reflectance spectra of metasurfaces of asymmetric Si-nanogap units are shown in Figure 4a, where the asymmetric parameter α was set to 10 in the unit cell. We note that the spectra for $n = 1.0$ are identical to those of $\alpha = 10$ in Figure 2a and that $y_1 = 185$ nm, $y_2 = 165$ nm, and $g = 50$ nm.

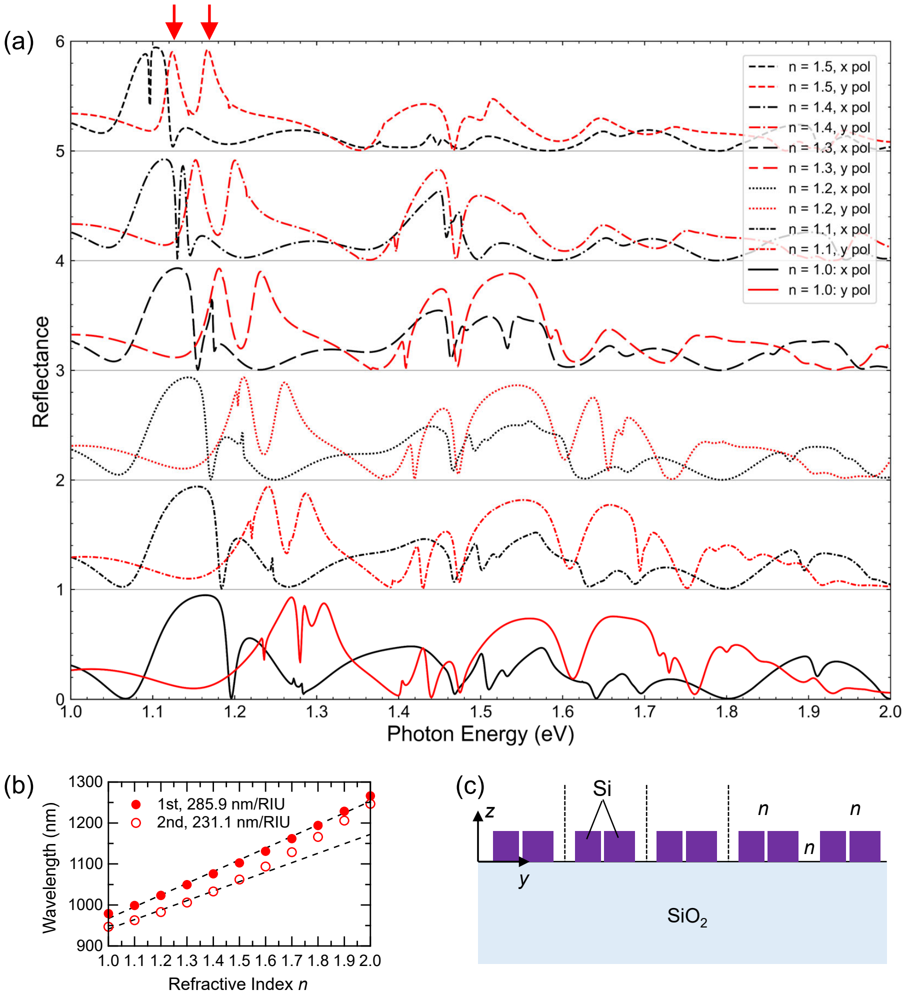

Figure 4. (**a**) Reflectance spectra dependent on refractive index n in the medium contacting the metasurface. Black and red curves show x- and y-polarized spectra, respectively, which are displayed with offset. Red arrows indicate a pair of resonances responsive to the index n over a wide range of $n = 1.0$–2.0. (**b**) Resonance shift of the pair of resonances. The first and second ones are shown with closed and open red circles, respectively. The slopes, fitted using a linear function and shown with dashed black lines, approximating performance as optical sensors in the units of nm/RIU. See more details in the text. (**c**) Schematic of a yz-section-view metasurface and medium of refractive index n. Dotted lines section the unit cell along the y axis.

Refractometric responses of the two resonances for $n = 1.5$, indicated by red arrows in Figure 4a, are plotted for the refractive index n over a range from 1.0 to 2.0 in Figure 4b, where the lower and higher energy peaks are shown with closed and open red circles, respectively. The wide range of the refractive index enables us to detect diverse materials from gas to liquid. Note that the vertical axis in Figure 4b is in the units of nm, which is inversely proportional to eV. The peaks were fitted using a linear function; dashed black lines represent the fitted line, reproducing the peak profiles over $n = 1.0$–1.5 in a good approximation; the first and second peaks plotted for the wavelength show refractometric responses of 285.9 and 231.1 nm/RIU, respectively. One of the advantages in the range of $n = 1.0$–1.5 is the approximately linear responsivity to the wide range.

Generally, refractometric responses can be fitted using quadratic functions [32] because dispersion relations between wavenumber and photon energy are mostly quadratic in 2D periodic systems. Indeed, the two peak profiles in Figure 4b can be traced for the whole range of $n = 1.0$–2.0 using quadratic functions.Thus, quantitative tracing of the two peaks is possible. Other various nanostructures including metasurfaces have been proposed as refractive-index sensors [26–28,32,43]; however, almost all of them do not guarantee such a wide-range responsivity and do have a narrow range of target, and are limited to a narrower range of targets than the present metasurface.

The medium of refractive index n is assumed to exist in the incident layer and gaps between the Si nanoblocks, as drawn in Figure 4c. Practically, liquid or gas media are assumed to be the target of refractive-index sensing. In addition, large molecules such as biomolecules can be detected as resonant shift, similarly to the conventional surface plasmon resonance method [44].

Figure 5 shows EM-field distributions at the two reflectance peaks at y polarization, indicated by the red arrows in Figure 4a. The peaks correspond to resonances responsive to the surrounding refractive index n. In Figure 5, the index n was set to 1.5.

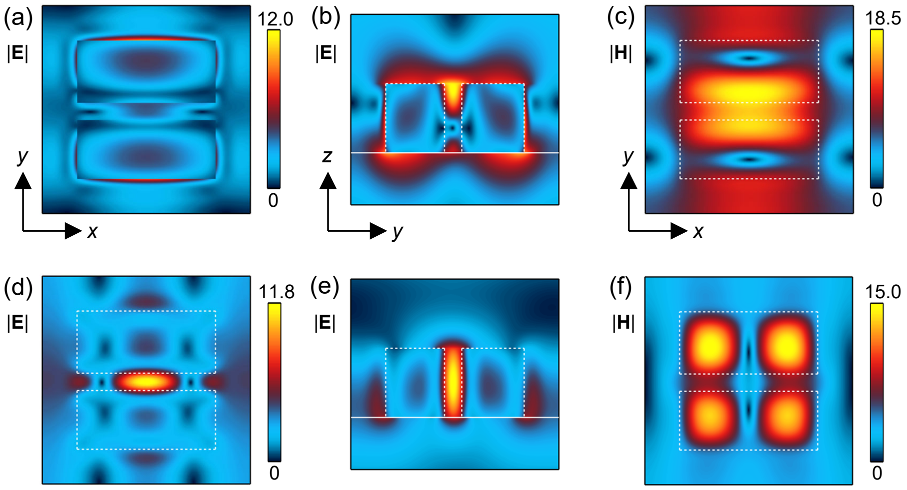

Figure 5. Resonant EM-field distributions on the two resonances responsive to surrounding refractive index, which is set to $n = 1.5$. (**a**,**b**) xy- and yz-section views of $|\mathbf{E}|$ distributions, respectively. The yz section cuts across the center of Si nanoblocks in the x direction. (**c**) $|\mathbf{H}|$ distribution in xy-section view. The photon energy is 1.124 eV in (**a**–**c**). (**d**–**f**) $|\mathbf{E}|$ and $|\mathbf{H}|$ distributions at 1.167 eV, displayed in a similar manner to (**a**–**c**). The incident polarization was set to $\mathbf{E}_{\text{in}} \parallel y$ in common. These xy sections are taken at the half-height of the Si-nanogap pair. The yz sections are through the center of the unit cell.

The first resonance at 1.124 eV is visualized in Figure 5a–c. The $|\mathbf{E}|$ component is presented in xy- and yz-section views, respectively. The color bar indicates the absolute values in common. A feature observed in the yz-section view is that the enhanced electric fields localize at the upper side of the nanogap. Since the xy section was taken at the half height of the Si nanoblocks, the enhanced electric fields are not seen; in contrast, the magnetic fields are enhanced on the xy section.

The second resonance at 1.167 eV is visualized in Figure 5d–f. The way of presentation is similar to that in Figure 5a–c. Obviously, the electric fields are enhanced at the nanogap. The magnetic fields are mostly localized in the Si nanoblocks.

From the enhanced electric-field distributions, the refractometric response in Figure 4a is most likely to originate from the locally enhanced electric fields at the nanogap in Figure 5, which are considered to enhance responses susceptible to the refractive index. Indeed, as shown in Figure A1, in a metasurface of symmetric Si nanoblock unit without any nanogap, resonances corresponding to the two resonances in the asymmetric metasurface (Figure 4) are not observed, and the refractometric response becomes small and is not found for a wide range of $n = 1.0$–1.5.

3.3. Nanogap Modes with Hugely Enhanced Electric Fields

Reflectance spectra of an asymmetric metasurface with $\alpha = 5$ and $g = 10$ nm are shown in Figure 6a. The sum of $y_1 + y_2 + g$ is set to 400 nm. The unit cell is the same dimension as that for Figure 2. The setting of incident wave is in common with that for Figure 3.

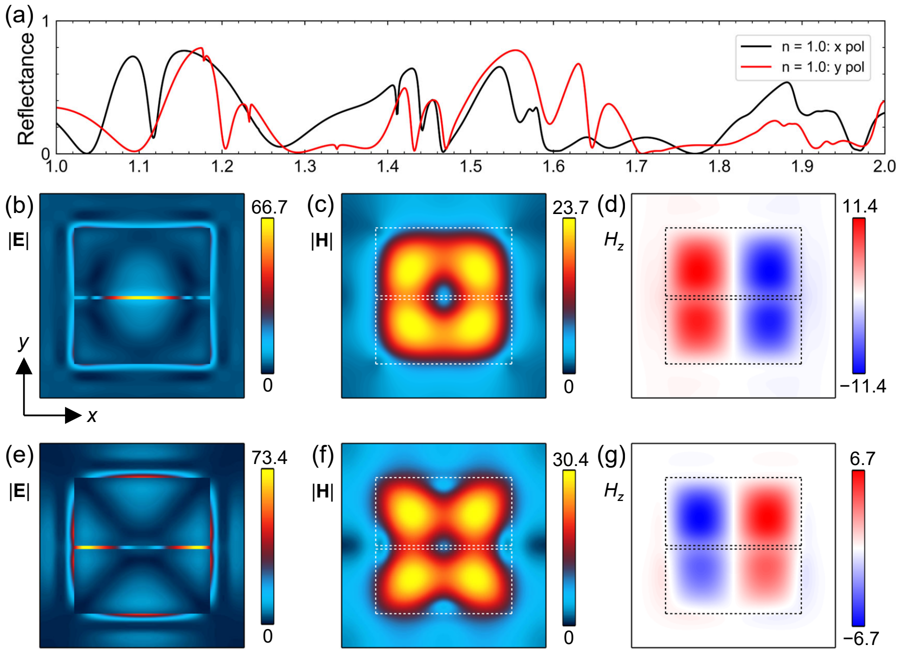

Figure 6. Optical resonances in an asymmetric metasurface of narrow gap $g = 10$ nm. (**a**) Reflectance spectra at x and y polarizations for refractive index $n = 1.0$, shown with black and red curves, respectively. (**b**–**d**) xy-section views of $|\mathbf{E}|$, $|\mathbf{H}|$, and snapshot of $\mathrm{Re}(H_z)$ at 1.178 eV, respectively. (**e**–**g**) xy-section views of $|\mathbf{E}|$, $|\mathbf{H}|$, and snapshot of $\mathrm{Re}(H_z)$ at 1.233 eV, respectively. The incident polarization was set to $\mathbf{E}_{\mathrm{in}} \parallel y$ in common. The xy sections were taken at the half-height of the Si-nanogap pair.

The reflectance spectrum in Figure 6a presents definite anisotropy for the incident x and y polarizations, shown with black and red curves, respectively. High-Q modes with narrow line widths appear at 1.178 and 1.233 eV at the y polarization, suggesting that they are qBIC modes. We examine the features in terms of the EM-field distributions in the following.

In Figure 6b–d, the resonant EM fields, $|\mathbf{E}|$, $|\mathbf{H}|$, and $\mathrm{Re}(H_z)$, are visualized, respectively, at the condition of the left arrow in Figure 4a, that is, 1.178 eV and y polarization. The EM fields are shown in a xy-section view of the unit cell; the section was taken at the half height of the Si-nanogap unit. The refractive index in the medium contacting the metasurface is set to 1.5. Evidently, strong localization of the electric field takes place at the Si nanogap, reaching the maximum of $|\mathbf{E}| = 66.7$ (or intensity $|\mathbf{E}|^2 = 4448.9$). In particular, the electric field localizes around the center of the nanogap. The magnetic field mainly distributes in the Si nanoblocks (Figure 6b) and the major component is found to be H_z (Figure 6d). The magnetic-field distribution indicates that this resonance is basically an MD mode. Introducing the nanogap, the electric field is able to localize inside the nanogap.

In Figure 6e–g, the resonant EM fields correspond to the condition of the right arrow in Figure 4a, that is, 1.233 eV and y polarization. The most prominent feature is seen at the electric-field distribution that has two maxima points regarding $|\mathbf{E}|$ in the nanogap. The maxima mean that the intensity $|\mathbf{E}|^2$ exceeds 5387, which is a huge enhancement, compared to the incidence of $|\mathbf{E}_{\mathrm{in}}|^2 = 1$. The magnetic field is qualitatively similar to that in Figure 6b,c. Thus, the two resonances in Figure 6 are basically MD modes associated with the first and second localized electric-field localizations in the nanogap.

This asymmetric metasurface of 10 nm gap can be compared to symmetric metasurfaces of Si-nanogap unit (Figure A2), which has a 10 nm gap. In the symmetric case, there is no qBIC mode, in contrast to the asymmetric case in Figure 6. Further details are described in Appendix A.

Regarding refractometric responses, the interaction volume with the surrounding medium becomes small in this asymmetric metasurface. Consequently, the responsiveness is similar to that in Figure A2, being quantitatively smaller than that in Figure 4a.

4. Discussion

Except for the qBIC modes, the metasurfaces have prominent optical resonances in the reflectance spectra. When the parameter $\alpha = 10$, it was found that the two gap modes emerge and are susceptible linearly to a wide range of refractive index of $n = 1.0$–1.5 (Figure 4a) and quadratically to a further wide range of $n = 1.0$–2.0 (Figure 4b); in the linear range, the responses were evaluated to be 286 and 231 nm/RIU. The two peaks of reflectance enable us to clearly identify the refractometric responses in the multi-peak reflectance spectra. Such a wide-range response has hardly been ensured for other metasurfaces, which are often limited to sensing for narrow refractive-index ranges [17,26–28,45–49]. Table 1 selectively lists the reported quantities based on Si-based nanostructures. Other platforms such as plasmonic structures were already addressed in other references [32,46–50].

Table 1. Comparison of Si metasurfaces and lattice in terms of refractive-index sensing. MSF, Exp, and R denotes metasurface, experiment, and reflectance, respectively. C band means a telecommunication band of 1530–1580 nm. Detected n ranges without any indication resulted from simulations.

Structure	Feature	Detected n	Response	Reference
Si MSF	2D array of 50 nm height pellets. Shift at 840–850 nm. 227 nm/RIU	1.33–1.35, Exp	Linear	[17]
Si MSF	qBIC at C band. Asymmetric Si bars. 440 nm/RIU	1.0–1.1	Linear	[26]
Si MSF	2D array of 450 nm height pairs. Shift at 1330–1600 nm. 612 nm/RIU	1.3–1.7	Linear	[27]
Si MSF	qBIC MD mode at C band. 30 nm nanogap. 258 nm/RIU	1.0–1.4	Linear	[28]
Si MSF	qBIC MD mode at C band. 30 nm nanogap. 317 nm/RIU	1.33–1.36, Exp	Linear	[28]
Si lattice	1D line and space. Large R change at 900–1000 nm	1.0–1.5 (wide)	Quadratic	[32]
Si lattice	2D square nanoblocks. Large R change at 745–790 nm	1.0–1.5 (wide)	Quadratic	[32]
Si MSF	qBIC MD mode at C band. Long-short bar pair. 231 nm/RIU	1.33–1.36, Exp	Linear	[43]
Si MSF	2D ring and bar unit. Shift at 1340–1360 nm. 289 nm/RIU	1.40–1.44, Exp	Linear	[45]
Si MSF	2D cylinders with thin spokes. Shift at 1381.99–1382.82 nm. 166 nm/RIU	1.000–1.005	Linear	[46]
Si lattice	1D grating of pedestal unit. Shift at 1480–1555 nm. 536 nm/RIU	1.33–1.47	Linear	[47]
Si MSF	qBIC at C band. 2D bar-pair unit. Shift at 1340–1360 nm. 501 nm/RIU	1.33–1.48	Linear	[48]
Si MSF	qBIC. Asymmetric Dimer. Shift at 710–760 nm. 140 nm/RIU	1.4–1.6, Exp	Linear	[49]

Table 1. *Cont.*

Structure	Feature	Detected n	Response	Reference
Si MSF	Asymmetric Si-nanogap unit. Shift at 950–1120 nm. 286, 231 nm/RIU	1.0–1.5 (wide)	Linear	This study
Si MSF	Asymmetric Si-nanogap unit. Shift at 950–1270 nm. Traceable double R peaks	1.0–2.0 (wide)	Quadratic	This study

As listed in Table 1, refractive index sensing was frequently studied for narrow ranges of the refractive index. In recent papers [26–28,43,48,49], qBIC modes were explored for refractive index sensing. Although the motives were to find highly sensitive refractive index sensors, the responses in the units of nm/RIU are competing with other resonant nanostructures. Indeed, the physical limit of refractive index sensors comprising periodic structures is given by Equation (1), indicating that the limit is proportional to the periodic length and that larger periodic lengths tend to exhibit larger sensitivity in nm/RIU. The performance of the qBIC-based sensors [26–28,43,48,49] is 20–70%, compared to the physical limit. Thus, there is a room to seek for better performance. Indeed, a 1D grating structure of a large periodic length of 820 nm showed an improved value of the sensitivity [47], compared with the qBIC-based sensors. The present metasurface sensors have a feature that they are responsive to a wide range of refractive indices, showing a practical potential. Other refractive index sensors using plasmonic lattices, optical fibers, and THz absorbers were discussed in a previous publication [32], where 569.1 nm/RIU was shown using a 1D plasmonic lattice and means 94.9% realization of the physical limit.

Regarding qBIC resonances, it is an experimental issue to obtain high-Q qBIC modes because nanofabricated metasurfaces have inevitable scattering loss that originates from roughness at the outermost surface of the nanostructures, even when Si is etched through a BOSCH process that allows for high-contrast, deep reactive ion etching of Si [43]; in fact, we refer to the fact that the experimental limitation for high-Q modes exists at Q $\approx$ 3000 in the Si-nanogap metasurfaces. In the structures described in this study, Q factors over 1000 will be a practical goal when experimentally pursuing the high-Q qBIC modes in the present Si-nanogap metasurfaces.

5. Conclusions

Metasurfaces of Si-nanogap units were numerically examined in this study. Introducing asymmetry in the unit cell, qBIC modes became detectable. As the asymmetric parameter α became larger, the qBIC signals in the reflectance spectra became evident. This is a feature of qBIC. Examining the resonant EM-field distributions, the EQ mode was observed at x polarization, and the MD and MQ modes were observed at y polarizations (Figure 2a). The MD modes were modified into two modes in accordance with the first and second electric-field nodes in the nanogap (Figure 6). Adjusting the gap g and the α, a huge electric-field-intensity enhancement exceeding 5000 was found. This is an outstanding feature in this all-dielectric metasurface. Considering application for refractive index sensing, the present metasurfaces are responsive to a very wide range of refractive indices from 1.0 to 2.0 (Figure 4). The linear approximation for sensitivity holds for $n = 1.0$–1.5, whereas the whole range of $n = 1.0$–2.0 is reproduced using quadratic functions. The changes in reflectance spectra are traceable and calibrated by measuring the pair of two reflectance peaks. Such a feature responding to the wide n range, to the best of our knowledge, has not been shown in other systems so far.

Funding: This study was partially supported by JSPS KAKENHI Grant Number JP24K01389.

Institutional Review Board Statement: Not applicable.

Informed Consent Statement: Not applicable.

Data Availability Statement: Data in this study are accessible upon reasonable request to the author.

Acknowledgments: The author thanks Keisuke Watanabe for discussion on Si-nanogap structures. Numerical implementations were conducted on supercomputers SX-AOBA in Cyberscience Center, Tohoku University, Japan.

Conflicts of Interest: The author declares no conflicts of interest.

Abbreviations

The following abbreviations are used in this manuscript:

qBIC	quasi-bound state in the continuum
SOI	Si-on-insulator
RCWA	rigrously coupled-wave analysis
S matrix	scattering matrix
MPI	multiparallel implementation
EM	electromagnetic
EQ	electric quadrupole
MD	magnetic dipole
MQ	magnetic quadrupole
FWHM	full-wave half maximum
Q factor	quality factor

Appendix A. Reflectance Spectra of Symmetric Metasurfaces

Here, we show two illustrative results using metasurfaces of symmetric units. In Figure A1, the unit has a single square Si nanoblock. In Figure A2, the unit has a symmetric Si pair. The refractometric responses are shown for comparison with Figure 4a.

Figure A1a shows the unit cell in a *xy*-section view, which is set to a dimension of 600 × 600 nm^2. The square Si nanoblock is 400 × 400 × 200 nm^3 in the unit cell located on the SiO$_2$ and Si base substrate, similarly to the unit cell in Figure 1.

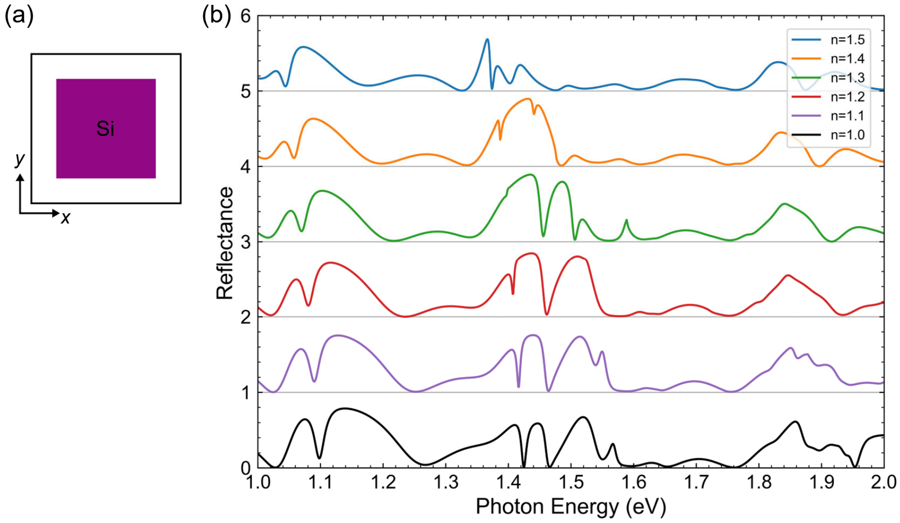

Figure A1. Reflectance spectra of metasurface of a single symmetric Si-nanoblock unit. The spectra depend on refractive index *n*. (**a**) Unit cell in *xy*-section view. (**b**) Reflectance spectra dependent on refractive index *n* in the contacting medium. They are displayed with offset.

Reflectance spectra for different refractive index *n* in the medium contacting the metasurface are shown in Figure A1b. The spectra exhibit small responsiveness to the refractive index, compared with the asymmetric metasurface in Figure 4a. This result indicates that the unit of a simple Si nanoblock is unsuitable for refractive index sensing.

Metasurface of symmetric Si-nanogap unit is tested in a configuration of refractive-index sensing. The unit structure has two Si nanoblocks of 400 × 200 × 200 nm^3, and the gap is set to 10 nm, as illustrated in Figure A2a. The Si-nanoblock pair is placed at the center of unit cell of 600 × 610 nm^2 in the xy plane and is assumed to be on the SiO_2 layer, similarly to Figure 1. The refractive index n changes from 1.0 to 1.5 in the medium in contact with the metasurface in Figure A2b.

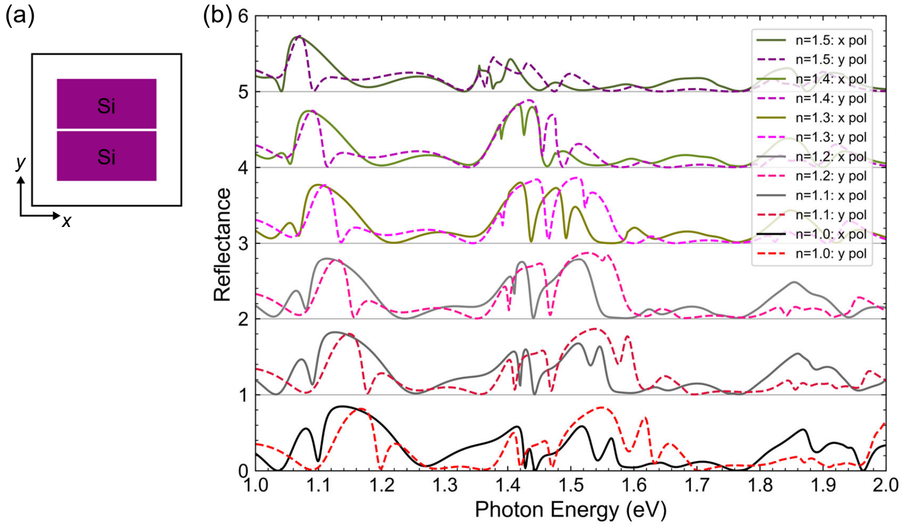

Figure A2. Reflectance spectra of metasurface of symmetric Si-nanogap unit. The spectra depend on refractive index n. (**a**) Unit cell in xy-section view. (**b**) Reflectance spectra dependent on refractive index n in the contacting medium. Solid and dashed curves indicate x- and y-polarized spectra, respectively. They are displayed with offset.

Response to refractive index n is evaluated for the y-polarization resonance that appears at 1.170 eV for $n = 1.0$, as shown with the red dashed curve in Figure A2. It turned out that the sensitivity is 193.6 nm/RIU, which is approximately 10% smaller than that of the asymmetric metasurface in Figure 4. This reduction probably comes from less enhanced EM fields in this symmetric Si-pair metasurface than that in the asymmetric metasurface (Figure 6); in particular, the maximum of $|\mathbf{E}|$ component in the nanogap of this symmetric metasurface is 10.9, which is approximately 16.3% of the maximum value in Figure 6a.

References

1. Yu, N.; Genevet, P.; Kats, M.A.; Aieta, F.; Tetienne, J.P.; Capasso, F.; Gaburro, Z. Light Propagation with Phase Discontinuities: Generalized Laws of Reflection and Refraction. *Science* **2011**, *334*, 333–337. [CrossRef]
2. Ni, X.; Kildishev, A.V.; Shalaev, V.M. Metasurface holograms for visible light. *Nat. Commun.* **2013**, *4*, 2807. [CrossRef]
3. Zheng, G.; Mühlenbernd, H.; Kenney, M.; Li, G.; Zentgraf, T.; Zhang, S. Metasurface holograms reaching 80% efficiency. *Nat. Nanotechnol.* **2015**, *10*, 308–312. [CrossRef]
4. Arbabi, A.; Horie, Y.; Bagheri, M.; Faraon, A. Dielectric metasurfaces for complete control of phase and polarization with subwavelength spatial resolution and high transmission. *Nat. Nanotechnol.* **2015**, *10*, 937–943. [CrossRef]
5. Sell, D.; Yang, J.; Doshay, S.; Yang, R.; Fan, J.A. Large-Angle, Multifunctional Metagratings Based on Freeform Multimode Geometries. *Nano Lett.* **2017**, *17*, 3752–3757. [CrossRef] [PubMed]
6. Fan, Z.; Shcherbakov, M.R.; Allen, M.; Allen, J.; Wenner, B.; Shvets, G. Perfect Diffraction with Multiresonant Bianisotropic Metagratings. *ACS Photonics* **2018**, *5*, 4303–4311. [CrossRef]
7. Chen, W.T.; Zhu, A.Y.; Sisler, J.; Huang, Y.W.; Yousef, K.M.A.; Lee, E.; Qiu, C.W.; Capasso, F. Broadband Achromatic Metasurface-Refractive Optics. *Nano Lett.* **2018**, *18*, 7801–7808. [CrossRef]
8. Khorasaninejad, M.; Chen, W.T.; Devlin, R.C.; Oh, J.; Zhu, A.Y.; Capasso, F. Metalenses at visible wavelengths: Diffraction-limited focusing and subwavelength resolution imaging. *Science* **2016**, *352*, 1190–1194. [CrossRef]
9. She, A.; Zhang, S.; Shian, S.; Clarke, D.R.; Capasso, F. Large area metalenses: Design, characterization, and mass manufacturing. *Opt. Express* **2018**, *26*, 1573–1585. [CrossRef] [PubMed]
10. Callewaert, F.; Velev, V.; Jiang, S.; Sahakian, A.V.; Kumar, P.; Aydin, K. Inverse-designed stretchable metalens with tunable focal distance. *Appl. Phys. Lett.* **2018**, *112*, 091102. [CrossRef]
11. Aiello, M.D.; Backer, A.S.; Sapon, A.J.; Smits, J.; Perreault, J.D.; Llull, P.; Acosta, V.M. Achromatic Varifocal Metalens for the Visible Spectrum. *ACS Photonics* **2019**, *6*, 2432–2440. [CrossRef]

12. Meem, M.; Banerji, S.; Pies, C.; Oberbiermann, T.; Majumder, A.; Sensale-Rodriguez, B.; Menon, R. Large-area, high-numerical-aperture multi-level diffractive lens via inverse design. *Optica* **2020**, *7*, 252–253. [CrossRef]
13. Horie, Y.; Han, S.; Lee, J.Y.; Kim, J.; Kim, Y.; Arbabi, A.; Shin, C.; Shi, L.; Arbabi, E.; Kamali, S.M.; et al. Visible Wavelength Color Filters Using Dielectric Subwavelength Gratings for Backside-Illuminated CMOS Image Sensor Technologies. *Nano Lett.* **2017**, *17*, 3159–3164. [CrossRef]
14. Chen, B.H.; Wu, P.C.; Su, V.C.; Lai, Y.C.; Chu, C.H.; Lee, I.C.; Chen, J.W.; Chen, Y.H.; Lan, Y.C.; Kuan, C.H.; et al. GaN Metalens for Pixel-Level Full-Color Routing at Visible Light. *Nano Lett.* **2017**, *17*, 6345–6352. [CrossRef]
15. Miyata, M.; Nakajima, M.; Hashimoto, T. High-Sensitivity Color Imaging Using Pixel-Scale Color Splitters Based on Dielectric Metasurfaces. *ACS Photonics* **2019**, *6*, 1442–1450. [CrossRef]
16. Zheng, R.; Wei, Y.; Zhang, Z.C.; Wang, Z.Y.; Ma, L.L.; Wang, Y.; Huang, L.; Lu, Y.Q. Stimuli-responsive active materials for dynamic control of light field. *Responsive Mater.* **2023**, *1*, e20230017. [CrossRef]
17. Yavas, O.; Svedendahl, M.; Dobosz, P.; Sanz, V.; Quidant, R. On-a-chip Biosensing Based on All-Dielectric Nanoresonators. *Nano Lett.* **2017**, *17*, 4421–4426. [CrossRef]
18. Tittl, A.; Leitis, A.; Liu, M.; Yesilkoy, F.; Choi, D.Y.; Neshev, D.N.; Kivshar, Y.S.; Altug, H. Imaging-based molecular barcoding with pixelated dielectric metasurfaces. *Science* **2018**, *360*, 1105–1109. [CrossRef]
19. Zhou, J.; Tao, F.; Zhu, J.; Lin, S.; Wang, Z.; Wang, X.; Ou, J.Y.; Li, Y.; Liu, Q.H. Portable tumor biosensing of serum by plasmonic biochips in combination with nanoimprint and microfluid. *Nanophotonics* **2019**, *8*, 307–316. [CrossRef]
20. Iwanaga, M. All-Dielectric Metasurface Fluorescence Biosensors for High-Sensitivity Antibody/Antigen Detection. *ACS Nano* **2020**, *14*, 17458–17467. [CrossRef] [PubMed]
21. Iwanaga, M. Robust Detection of Cancer Markers in Human Serums Using All-Dielectric Metasurface Biosensors. *Biosensors* **2023**, *13*, 377. [CrossRef] [PubMed]
22. Iwanaga, M.; Hironaka, T.; Ikeda, N.; Sugasawa, T.; Takekoshi, K. Metasurface Biosensors Enabling Single-Molecule Sensing of Cell-Free DNA. *Nano Lett.* **2023**, *23*, 5755–5761. [CrossRef] [PubMed]
23. Fu, Q.; Iwanaga, M.; Tang, Y. Metasurface Platform Incorporating Aggregation Induced Emission Based Biosensor for Enhanced Human Serum Albumin Detection. *Adv. Opt. Mater.* **2024**, *12*, 2400868. [CrossRef]
24. Von Neumann, J.; Wigner, E. Über merkwürdige diskrete Eigenwerte. *Phys. Z.* **1929**, *30*, 465–467.
25. Hsu, C.W.; Zhen, B.; Lee, J.; Chua, S.L.; Johnson, S.G.; Joannopoulos, J.D.; Soljačić, M. Observation of trapped light within the radiation continuum. *Nature* **2013**, *499*, 188–191. [CrossRef]
26. Ndao, A.; Hsu, L.; Cai, W.; Ha, J.; Park, J.; Contractor, R.; Lo, Y.; Kanté, B. Differentiating and quantifying exosome secretion from a single cell using quasi-bound states in the continuum. *Nanophotonics* **2020**, *9*, 1081–1086. [CrossRef]
27. Hsiao, H.H.; Hsu, Y.C.; Liu, A.Y.; Hsieh, J.C.; Lin, Y.H. Ultrasensitive Refractive Index Sensing Based on the Quasi-Bound States in the Continuum of All-Dielectric Metasurfaces. *Adv. Opt. Mater.* **2022**, *10*, 2200812. [CrossRef]
28. Watanabe, K.; Iwanaga, M. Nanogap enhancement of the refractometric sensitivity at quasi-bound states in the continuum in all-dielectric metasurfaces. *Nanophotonics* **2023**, *12*, 99–109. [CrossRef]
29. Kodigala, A.; Lepetit, T.; Gu, Q.; Bahari, B.; Fainman, Y.; Kanté, B. Lasing action from photonic bound states in continuum. *Nature* **2017**, *541*, 196–199. [CrossRef]
30. Ha, S.T.; Fu, Y.H.; Emani, N.K.; Pan, Z.; Bakker, R.M.; Paniagua-Domínguez, R.; Kuznetsov, A.I. Directional lasing in resonant semiconductor nanoantenna arrays. *Nat. Nanotechnol.* **2018**, *13*, 1042–1047. [CrossRef]
31. Liu, Z.; Xu, Y.; Lin, Y.; Xiang, J.; Feng, T.; Cao, Q.; Li, J.; Lan, S.; Liu, J. High-Q Quasibound States in the Continuum for Nonlinear Metasurfaces. *Phys. Rev. Lett.* **2019**, *123*, 253901. [CrossRef] [PubMed]
32. Iwanaga, M. A Design Strategy for Surface Nanostructures to Realize Sensitive Refractive-Index Optical Sensors. *Nanomaterials* **2023**, *13*, 3081. [CrossRef] [PubMed]
33. Palik, E.D. *Handbook of Optical Constants of Solids II*; Academic: San Diego, CA, USA, 1991.
34. Li, L. New formulation of the Fourier modal method for crossed surface-relief gratings. *J. Opt. Soc. Am. A* **1997**, *14*, 2758–2767. [CrossRef]
35. Li, L. Formulation and comparison of two recursive matrix algorithm for modeling layered diffraction gratings. *J. Opt. Soc. Am. A* **1996**, *13*, 1024–1035. [CrossRef]
36. Christ, A.; Tikhodeev, S.G.; Gippius, N.A.; Kuhl, J.; Giessen, H. Waveguide-Plasmon Polaritons: Strong Coupling of Photonic and Electronic Resonances in a Metallic Photonic Crystal Slab. *Phys. Rev. Lett.* **2003**, *91*, 183901. [CrossRef]
37. Christ, A.; Zentgraf, T.; Tikhodeev, S.G.; Gippius, N.A.; Kuhl, J.; Giessen, H. Controlling the interaction between localized and delocalized surface plasmon modes: Experiment and numerical calculations. *Phys. Rev. B* **2006**, *74*, 155435. [CrossRef]
38. Christ, A.; Ekinci, Y.; Solak, H.H.; Gippius, N.A.; Tikhodeev, S.G.; Martin, O.J.F. Controlling the Fano interference in a plasmonic lattice. *Phys. Rev. B* **2007**, *76*, 201405. [CrossRef]
39. Iwanaga, M. Polarization-selective transmission in stacked two-dimensional complementary plasmonic crystal slabs. *Appl. Phys. Lett.* **2010**, *96*, 083106. [CrossRef]
40. Iwanaga, M.; Choi, B. Heteroplasmon Hybridization in Stacked Complementary Plasmo–Photonic Crystals. *Nano Lett.* **2015**, *15*, 1904–1910. [CrossRef]
41. Iwanaga, M. All-Dielectric Metasurfaces with High-Fluorescence-Enhancing Capability. *Appl. Sci.* **2018**, *8*, 1328. [CrossRef]

42. Koshelev, K.; Lepeshov, S.; Liu, M.; Bogdanov, A.; Kivshar, Y. Asymmetric Metasurfaces with High-Q Resonances Governed by Bound States in the Continuum. *Phys. Rev. Lett.* **2018**, *121*, 193903. [CrossRef] [PubMed]
43. Watanabe, K.; Iwanaga, M. Optimum asymmetry for nanofabricated refractometric sensors at quasi-bound states in the continuum. *Appl. Phys. Lett.* **2024**, *124*, 111705. [CrossRef]
44. Homola, J.; Koudela, I.; Yee, S.S. Surface plasmon resonance sensors based on diffraction gratings and prism couplers: Sensitivity comparison. *Sens. Actuator B-Chem.* **1999**, *54*, 16–24. [CrossRef]
45. Yang, Y.; Kravchenko, I.I.; Briggs, D.P.; Valentine, J. All-dielectric metasurface analogue of electromagnetically induced transparency. *Nat. Commun.* **2017**, *5*, 5753. [CrossRef]
46. Tognazzi, A.; Rocco, D.; Gandolfi, M.; Locatelli, A.; Carletti, L.; De Angelis, C. High Quality Factor Silicon Membrane Metasurface for Intensity-Based Refractive Index Sensing. *Optics* **2021**, *2*, 193–199. [CrossRef]
47. Beliaev, L.Y.; Stounbjerg, P.G.; Finco, G.; Bunea, A.I.; Malureanu, R.; Lindvold, L.R.; Takayama, O.; Andersen, P.E.; Lavrinenko, A.V. Pedestal High-Contrast Gratings for Biosensing. *Nanomaterials* **2022**, *12*, 1748. [CrossRef]
48. Liu, Z.; Guo, T.; Tan, Q.; Hu, Z.; Sun, Y.; Fan, H.; Zhang, Z.; Jin, Y.; He, S. Phase Interrogation Sensor Based on All-Dielectric BIC Metasurface. *Nano Lett.* **2023**, *23*, 10441–10448. [CrossRef]
49. Van Loon, T.; Liang, M.; Delplace, T.; Maes, B.; Murai, S.; Zijlstra, P.; Rivas, J.G. Refractive index sensing using quasi-bound states in the continuum in silicon metasurfaces. *Opt. Express* **2024**, *32*, 14289–14299. [CrossRef]
50. Qin, J.; Jiang, S.; Wang, Z.; Cheng, X.; Li, B.; Shi, Y.; Tsai, D.P.; Liu, A.Q.; Huang, W.; Zhu, W. Metasurface Micro/Nano-Optical Sensors: Principles and Applications. *ACS Nano* **2022**, *16*, 11598–11618. [CrossRef]